PHOTONICS Research

Emerging photoluminescence from defective vanadium diselenide nanosheets

Amir Ghobadi,[1,2,5] Turkan Gamze Ulusoy Ghobadi,[3] Ali Kemal Okyay,[2,3] and Ekmel Ozbay[1,2,3,4,*]

[1]NANOTAM-Nanotechnology Research Center, Bilkent University, 06800 Ankara, Turkey
[2]Department of Electrical and Electronics Engineering, Bilkent University, 06800 Ankara, Turkey
[3]UNAM-Institute of Materials Science and Nanotechnology, Bilkent University, 06800 Ankara, Turkey
[4]Department of Physics, Bilkent University, 06800 Ankara, Turkey
[5]e-mail: amir@ee.bilkent.edu.tr
*Corresponding author: ozbay@bilkent.edu.tr

Received 12 December 2017; revised 17 January 2018; accepted 21 January 2018; posted 23 January 2018 (Doc. ID 315573); published 22 March 2018

In this paper, for the first time to our knowledge in the literature, we demonstrate photoluminescence from two-dimensional (2D) vanadium diselenide (VSe_2) nanosheets (NSs). The preparation of these nanostructures is carried out with a combinational method based on nanosecond pulsed laser ablation (PLA) and chemical exfoliation. For this aim, VSe_2 bulk is first ablated into nanoparticles (NPs) inside a water solution. Afterward, NPs are chemically exfoliated into NSs using lithium intercalation via ultrasonic treatment. Although VSe_2 is a semimetal in its bulk form, its nanostructures show photo-responsive behavior, and it turns into a strongly luminescent material when it is separated into NSs. Based on the obtained results, the surface defects induced during the PLA process are the origin of this photoluminescence from NSs. Our findings illustrate that this new material can be a promising semiconductor for photovoltaic and light emitting diode applications.

OCIS codes: (130.5990) Semiconductors; (160.4670) Optical materials; (250.5230) Photoluminescence.

https://doi.org/10.1364/PRJ.6.000244

1. INTRODUCTION

The discovery of the intriguing electrical and physical properties of two-dimensional (2D) materials [1–3], such as graphene, has inspired scientists to synthesize other new types of 2D materials. Transition metal dichalcogenides (TMDs) are one kind of these recently explored materials and have been strikingly highlighted in recent years [4–8]. Unlike graphene, which is inherently a semimetal with zero optical band gap, TMDs can show diverse bulk properties from insulators (HfS_2), semiconductors (MoS_2, WS_2), and semimetals (WTe_2, $TiSe_2$), to true metals (NbS_2, VSe_2). For this reason, in recent years, TMDs have been promising building blocks for a wide range of applications, including photovoltaics [9–11], photo detectors [12–14], light emitting diodes (LEDs) [15,16], and photo-electrochemical systems [17–20]. In fact, the fascinating properties of TMDs can be revealed as they are thinned into a monolayer or to a few layers thickness. The conversion from an indirect to a direct band-gap semiconductor is one of these prominent differences between the bulk and monolayer TMDs. This phenomenon is due to quantum confinement effects and has been found in different types of TMDs such as MoS_2 [21,22], WS_2 [23], WSe_2 [24,25], and $MoTe_2$ [26–28]. This conversion makes 2D TMDs an excellent choice for LED applications in the visible (Vis) and near infrared (NIR) spectral regimes. Several different strategies have also been employed to intensify and tune the photoluminescence (PL) from 2D TMDs. Chemical treatments [29–31], alloying [32–35], coupling with surface plasmon polaritons [36,37], integration with photonic crystal cavities [38,39], and strain engineering [40] are some of these proposed methodologies to improve the band-to-band PL characteristics of 2D TMDs. Moreover, it is found that a strong sub-band-gap PL can be originated from defect-mediated transitions [23,25,41–46] that are of great interest in the design of NIR LEDs.

Vanadium diselenide (VSe_2) is another member of this family that belongs to group five TMDs. Bulk VSe_2 is a layered compound whose crystal structure is based upon strongly covalent (intralayer) Se–V–Se bonds within each layer and weak van der Waals (interlayer) Se…Se interactions in between. Compared to other types of TMDs, the existence of an overlap between the valance band (VB) and conduction band (CB) of VSe_2 makes this material a pure metal, and it possesses a high level of electrical conductivity that is a

key factor in optoelectronics applications [47–49]. Besides the extra-high electrical conductivity of a VSe_2 monolayer (that has been experimentally proved recently [47]), some other unexpected properties of this material have also been investigated in recent years. Its unique charge density wave (CDW) [50], ferromagnetism behavior [51–53], and electrochemical activity [toward a hydrogen evolution reaction (HER)] [54–58] are examples of these explorations. Owing to its metallic nature with no optical band gap, it has been expected that it should not be considered for optical applications. Very recently, density functional theory (DFT) calculations revealed that both bulk 2H-VSe_2 and 1T-VSe_2 and monolayers of H-VSe_2 and T-VSe_2 are thermodynamically stable [48]. These DFT calculations demonstrated that although T-VSe_2 is a pure metal, H-VSe_2 is a semimetal with no band gap. However, considering spin-up or spin-down bands separately, H-VSe_2 introduces a small band gap around 0.8 eV between the valance band maximum (VBM) and conduction band minimum (CBM). As the only report on optical behavior of VSe_2, He *et al.* attained an excellent photocatalytic activity toward methyl orange degradation from bulk VSe_2 [59].

Another factor that limits the functionality of VSe_2 is its synthetic challenge. Other types of nanostructured TMDs, such as luminescent MoS_2 quantum dots and nanosheets, can be obtained with a variety of controllable synthesis methods, such as chemical vapor deposition (CVD) [21,22] and sonication-assisted liquid exfoliation [60–64]. However, for the case of VSe_2, researchers could only realize it by chemical vapor transport (CVT) [65–67], CVD [47,68], and Scotch-tape-based mechanical exfoliation [54] of the bulk VSe_2, until Xu *et al.* [53] recently synthesized it in an aqueous solution. Later, other researchers have also proposed different chemical-based synthesis methods to make VSe_2 nanosheets [55,59]. However, due to the complex chemical environment in solution, it is still challenging to prepare contamination-free samples by a solution-based method. One of the facial and large-scale-compatible methods that has been recently used to synthesize quantum dots (QDs) from TMDs and other 2D materials such as graphene is pulsed laser ablation (PLA) [69–72]. We have recently demonstrated that by tuning the laser fluence, blue and green ultra-small luminescent silicon QDs can be synthesized [73]. However, up to now, there is no report on the synthesis of VSe_2 nanostructures using PLA.

In this paper, we propose a top–down, large-scale-compatible, surfactant-free, and widely adopted approach to synthesize VSe_2 nanostructures (directly from the rock) by utilizing a two-stage process. In the first stage, the nanosecond PLA technique is utilized to produce three-dimensional (3D) VSe_2 nanoparticles (NPs) from its bulk. Following this step, the ultra-sonication-assisted lithium intercalation process is conducted using lithium carbonate in a colloidal solution of NPs to successfully produce 2D VSe_2 nanosheets (NSs). During this process, ultra-sonication assists lithium ions to easily permeate into the VSe_2 matrix and break the weak van der Waals interaction between the stacked layers. Afterward, the structural and optical characterizations are conducted on the NP and NS samples. Our findings show that while the VSe_2 rock is a metallic material with no band gap, the resultant NPs and NSs are photo-responsive. It has been shown that NPs have an effective band gap of 1.75 eV, and this value gets wider to an amount of 3.45 eV for the case of NSs. However, the main difference between NP and NS morphologies is raised from their PL properties. While NPs possess a weak emission at the Vis-NIR regimes, NSs have a strong emission with a peak located at around 710 nm. From these findings, it can be speculated that moving from 3D NPs to 2D NSs, a transition from the indirect to direct band gap takes place. Moreover, the experimental characterizations elucidate the fact that this emission is mainly originated from defect-mediated transitions. The origin of all the above-mentioned phenomena has been scrutinized and discussed in this study. To the best of our knowledge, this is the first report on the synthesis of luminescent VSe_2 NSs where its facile and contaminant-free preparation route makes the upscaling possible. Besides its inherently high electrical properties, this report proves that VSe_2 can also provide a superior optical response, which makes it a potential material for future optoelectronic applications.

2. EXPERIMENTS

A. VSe_2 Nanoparticle Synthesis

For the synthesis of VSe_2 NPs, the PLA method was employed similar to our previously reported study [73]. Briefly, a Nufern NuQ fiber laser (NUQA-1064-NA-0030-F1) operating at ambient temperature with a beam wavelength of 1064 nm, pulse duration of 100 ns, repetition rate/frequency of 30 kHz, and a pulse energy of 1 mJ was utilized for the process. To synthesize the VSe_2 colloidal nanoparticles, pure VSe_2 rock is used as a bulk target that is immersed in deionized water. The laser beam scans the VSe_2 target (in an active area of 1 cm^2) with a spot size of approximately 3.8 mm in diameter using a 200 mm focal length taking into account the refraction through the water. The laser ablation scan pattern is chosen to be an inward spiral. The reason is the fact that, in spiral scanning, the ablated nanoparticles in each step are collected toward the center and re-ablated in the next cycles. Considering the fact that ablation was carried out for 300 loops (at a fluence amount of 50 mJ/cm^2), it is expected that the produced NPs would undergo several melting/re-solidifying cycles, and this in turn leads to the formation of defective small NPs. The output of the PLA is an orange-colored solution.

B. VSe_2 Nanosheet Synthesis

The intercalation reactions are performed by adding 10 mg Li_2CO_3 into 2 mL VSe_2 NPs solution, which is roughly a molar Li excess of 2:1. Then, the lithium intercalation is facilitated by applying ultra-sonication for 1.5 h. The duration of sonication is chosen based on the color of the NS solution. We found that after this duration, the color of solution is turned into a homogeneous transparent gray.

C. Material Characterization

To characterize the structural properties of the synthesized VSe_2 NPs and NSs, a scanning electron microscope (SEM, FEI—Quanta 200 FEG) operated at 10 kV and a transmission electron microscope (TEM, Tecnai G2-F30, FEI) operated at 200 kV are employed. For TEM and high-resolution TEM (HRTEM) measurements, a few droplets of the solution

are drop-casted on the copper grid. To conduct elemental and surface analysis, an X-ray photoelectron spectroscopy (XPS, Thermoscientic K-Alpha, Al K-Alpha radiation, $h\nu = 1486.6$ eV) measurement has been performed at the survey mode by operating a flood gun to prevent surface charging with the pass energy and step size set to 30 eV and 0.1 eV, respectively. Peak positions were calibrated by referencing the C1s peak position (284.8 eV), and other peaks are shifted in the spectrum accordingly. Powder X-ray diffraction (PXRD) has been carried out by Panalytical X'pert Multi-Purpose, and the patterns have been collected in the range of $2\theta = 10°$–$70°$ using Bragg–Brentano geometry (Cu Kα radiation). The VSe_2 solutions were drop-casted onto the sheet of thin glass at room temperature. Finally, the height profile and layer thickness are evaluated from the tapping mode in atomic force microscopy (AFM, PSIA).

D. Optical Characterization

In order to optically characterize nanoparticles, an ultraviolet–visible–near-infrared (UV-Vis-NIR) spectrophotometer (Cary 5000, Varian) is employed to obtain the absorption response of the samples. The emission characteristics of the NPs have been examined by employing PL measurements using the Cary Eclipse Fluorescence Spectrophotometer with an excitation wavelength of 330 nm. The emission spectra are recorded between 600 nm and 900 nm.

3. RESULTS AND DISCUSSION

Figure 1 depicts the preparation steps of VSe_2 NPs and NSs. As this schematic representation explains, first, VSe_2 rock is ablated using a nanosecond-pulsed NIR laser beam. The obtained NP solution (inside the water) has an orange-like color. Afterward, lithium carbonate powder is added to the solution of NPs. To facilitate the lithium intercalation process, ultrasonication is applied to the solution for 1.5 h. As the output of this liquid phase exfoliation, a transparent gray solution of VSe_2 NSs would be formed. To explore the formation and structural properties of the resultant VSe_2 nanostructures, the obtained solutions are drop-casted on a copper grid, and TEM imaging is conducted on them. Figure 2(a) clearly illustrates the formation of spherical NPs with a relatively wide distribution that is mainly characteristic of the PLA method. The transformation of these 3D NPs to 2D NSs has been confirmed in Fig. 2(b). Looking at HRTEM images [Fig. 2(c)], it can be deduced that the VSe_2 NSs are single crystalline with a lattice spacing around 2.6 Å that is characteristic of the (011) plane of VSe_2 [55]. Moreover, the SEM image of the drop-casted NS sample [Fig. 2(d)] is also showing the layered morphology of the sample. To further confirm the VSe_2 NSs' thickness, an AFM measurement is employed on the drop-casted NS sample, as depicted in Fig. 2(e). The AFM measurement results show a step-like profile in which the size of each step is equal to 0.33 nm, which is equal to the thickness of the VSe_2 monolayer [52,55]. Therefore, all the aforementioned characterizations prove the successful synthesis of VSe_2 NPs and NSs. To have a better comparison, XRD measurement is performed to evaluate the NSs response in higher volumes rather than a single unit (as we analyzed in TEM and AFM images). Figure 3 shows the XRD patterns for three cases of VSe_2 rock, NP, and NS. As this figure implies, the bulk material displays several peaks originated from the reflection of different lattice planes. In this case, four main intense peaks can be recorded that correspond to (001), (002), (003), and (004) planes in the bulk rock. However, when the materials are thinned to the NS design, most of these peaks disappear, and only a single intense peak corresponds to the (011) plane. The removal of the other peaks in the XRD pattern explains that the synthesis of mono- or few-layer NSs has been successfully made through the liquid phase exfoliation step. No XRD signal was recorded for NPs due to the ultra-small dimensions of these particles [61].

To optically characterize the produced NPs and NSs, UV-Vis-NIR spectroscopy is carried out in these samples. The absorption spectra of these samples have been depicted in Fig. 4(a). Interestingly, both synthesized NPs and NSs are photo-responsive, which is in contrast with our expectation of having pure metallic 1T VSe_2 with no band gap. Therefore, this shows that applying laser ablation into the bulk rock is responsible for this phenomenon. An earlier study has proved that a phase transition from 1T- to 2H-MoS_2 can occur upon

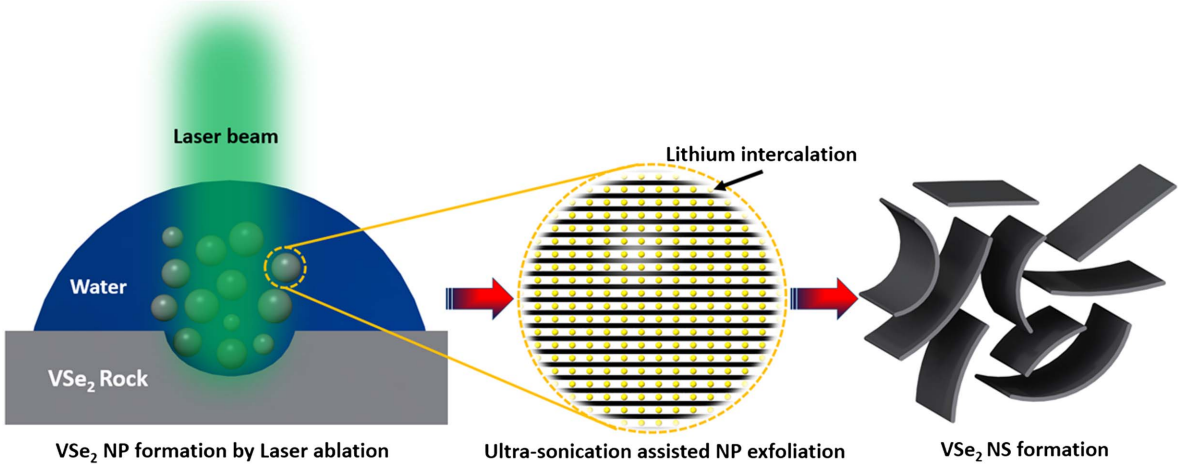

Fig. 1. Schematic representation of VSe_2 NP and NS formation using the PLA and ultra-sonication-assisted chemical exfoliation.

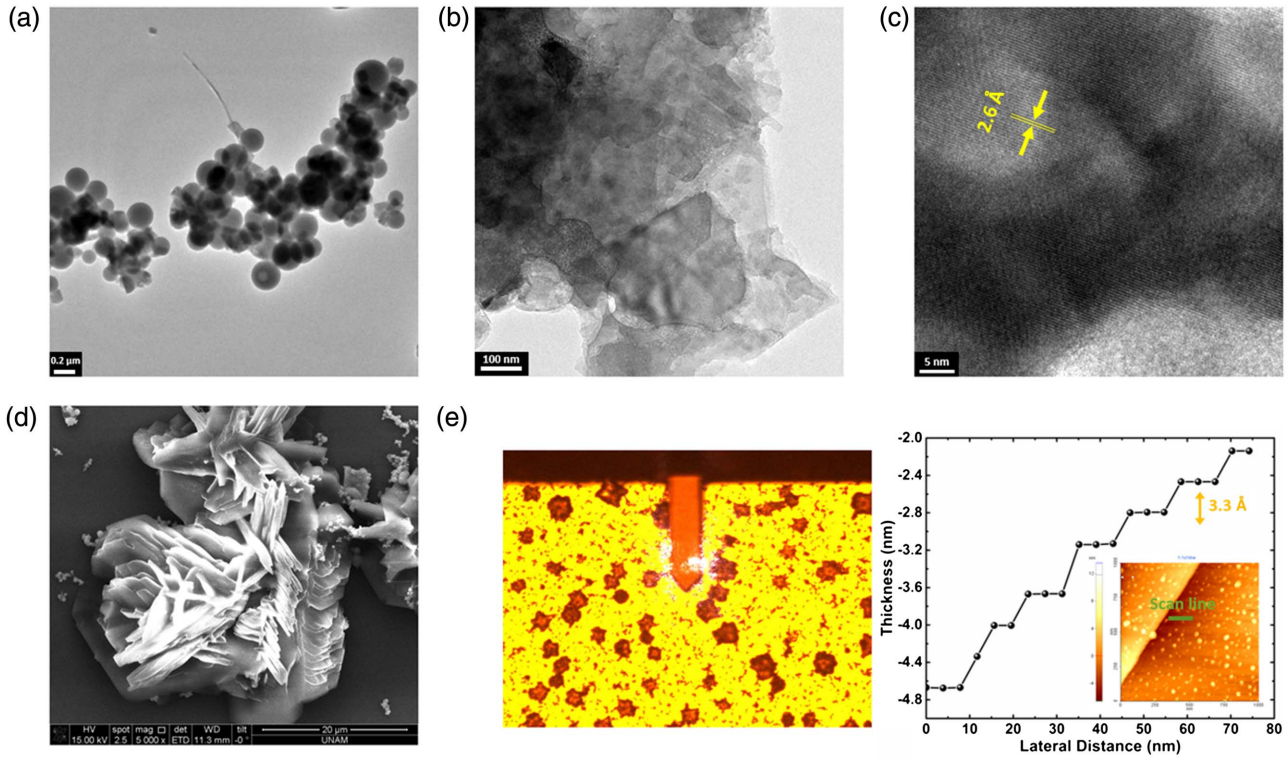

Fig. 2. TEM images showing the successful formation of (a) laser-ablated NPs and (b) chemically exfoliated NSs. (c) HRTEM image showing the lattice spacing in the synthesized NSs. (d) SEM image of the drop-casted NS solution. (e) AFM measurement results showing the formation of single to a few layers of VSe_2 and its thickness profile.

exposure of the MoS_2 bulk into IR laser irradiation [60]. Considering the fact that the PLA process is done with an IR laser beam at 1064 nm, it is speculated that, during this step, a phase transformation from 1T to 2H can take place, as shown in Fig. 4(b). According to DFT calculations, while 1T-VSe_2 is a pure metal, 2H-VSe_2 takes a semimetal behavior in which, considering spin-up or spin-down bands separately, a narrow band gap can be assigned to this phase of VSe_2 [48,49]. Looking back to the absorption responses of the NPs' and NSs' solutions, one can clearly find that the absorption of VSe_2 NPs has been extended above 700 nm, while this response is limited to wavelengths below 360 nm for the case of NSs. In other words, in moving from 3D NPs to 2D NSs, VSe_2 experiences a band-gap widening. As already mentioned, a similar behavior has been already revealed for other semiconducting TMD types, such as MoS_2, WS_2, and WSe_2, where moving from a 3D bulk design to a 2D monolayer (or a few layers) introduces a band-gap widening with a direct transition of excitons from CBM to VBM. To have a better qualitative comparison, the band gaps of both solutions have been estimated by the extrapolation of the linear part of the $(\alpha\omega)^{1/2}$ versus the $h\nu$ axis in the energy range of 1.5–6 eV [as depicted in the inset of Fig. 4(a)]. Based on these results, while the NPs of VSe_2 have a band gap of 1.75 eV, this band gap gets wider up to a value of 3.45 eV for the NSs case. This can also be understood from the color of both solutions. As Fig. 5(a) clearly exhibits, the VSe_2 NPs solution has an orange-like color, while the NSs solution has a transparent gray appearance. However, a fascinating phenomenon can be probed upon the excitation of these solutions with an ultraviolet (UV) light. As this figure clearly shows, the NS

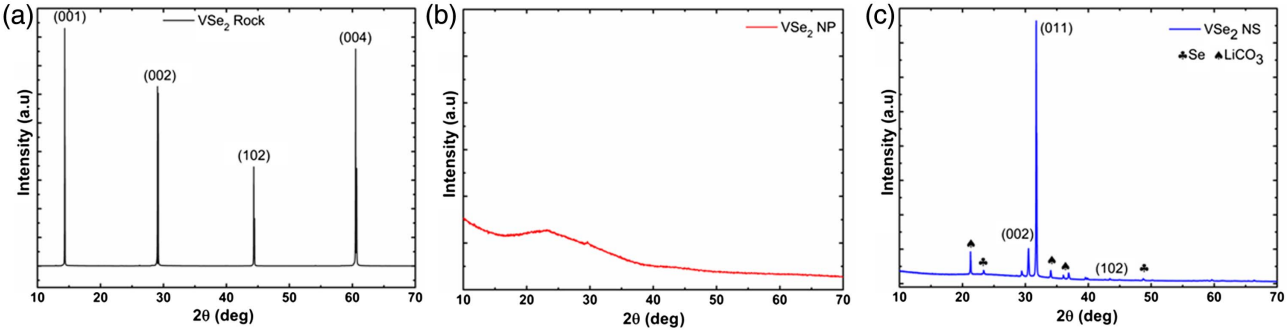

Fig. 3. XRD patterns of the VSe_2 (a) rock, and produced (b) NP and (c) NS samples.

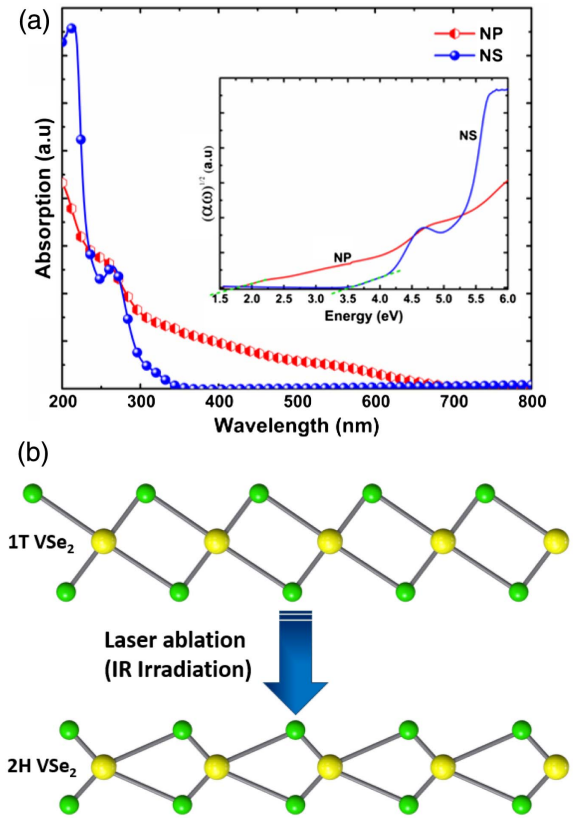

Fig. 4. (a) Absorption spectra of the synthesized colloidal NPs and NSs. The inset estimates the optical band gap of the samples. (b) The transition from 1T phase to 2H phase in IR radiated VSe_2 samples.

solution gets a red color and demonstrates the existence of PL in this case. To have a better picture from the emission behavior of the samples, we have performed PL spectroscopy measurements for both samples. Taking the band gaps of both samples into account, the excitation wavelength has been chosen to be 330 nm. Figure 5(b) shows the PL spectra of both the NP and NS samples. According to this figure, the NS sample has a strong PL intensity with two peaks at 710 nm and 830 nm where the first one is much stronger. On the other side, NPs also represent a similar PL pattern but with much weaker intensities. In order to explore the origin of these emissions, as the first assumption, it can be speculated that this is due to indirect to direct band-gap transformation. However, the emission spectra are located at much lower energies than the direct band-to-band transition of the NS sample. In other words, although there was no detectable emission at the vicinity of the NSs' band gap, a strong sub-band-gap emission can be attained from this sample. On the other hand, the similar PL patterns for both the NP and NS cases induce the fact that these emission profiles are not due to the 3D-to-2D shape transformation of the VSe_2. Another possible mechanism for the emission of VSe_2 NSs can be assigned to quantum confinement in their lateral dimension where NSs are broken into small pieces during the ultra-sonication step. It is well known that as a dimension of a semiconductor takes values as small as its exciton Bohr radius, much stronger PL can be accomplished. To evaluate this statement, we have excited the NS solution with four different wavelengths of 300, 330, 360, and 370 nm. Apart from 370 nm, which is smaller than the band gap of the NSs, all the other excitation wavelengths cause strong PL from the sample. This figure distinctly implies that

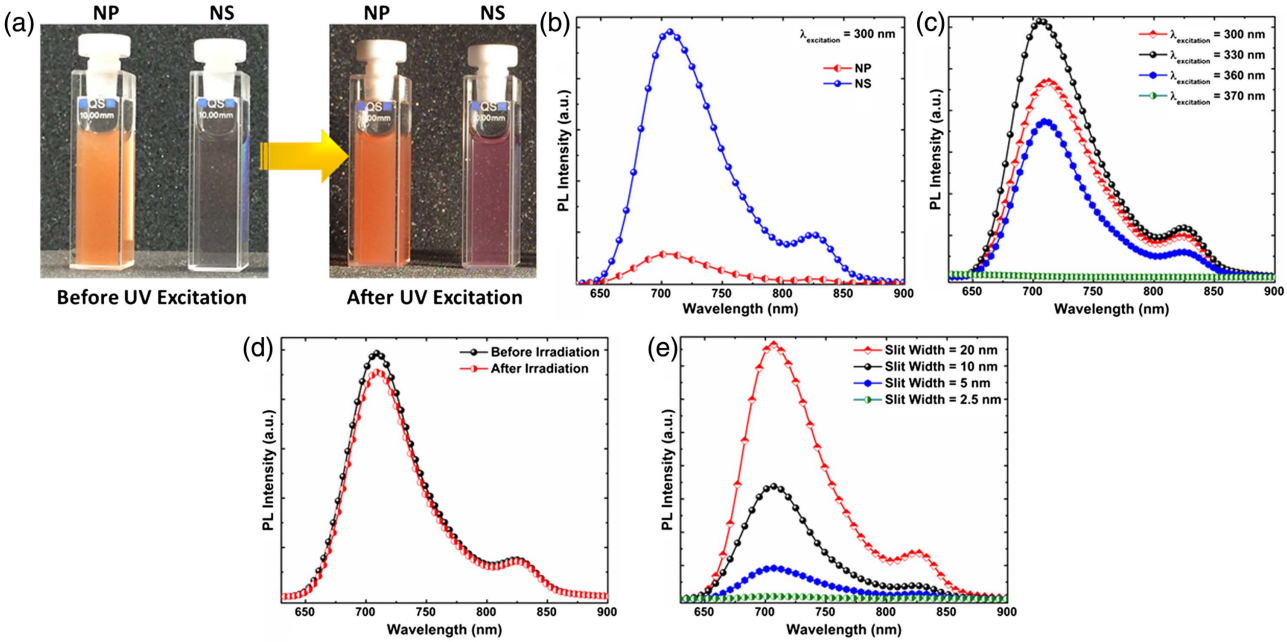

Fig. 5. (a) Images of the NP and NS solutions before and after excitation with UV-incident light and (b) their PL spectra upon excitation with a 300 nm light. (c) The change of the emission spectra of the NS sample under different excitation wavelengths. (d) PL spectra change after irradiation with continuous light for 4 h. (e) The dependence of PL on the excitation light intensity at an excitation wavelength of 330 nm with different slit width values.

the locations of the PL peaks do not experience any change upon the excitation of a different wavelength. However, considering the wide size distribution of VSe_2 NSs, which is a result of the formation of different-sized PLA NPs, if this mechanism is responsible for this emission, it is expected that the position of the peak should change under different excitation wavelengths. Therefore, this hypothesis also fails to explain the origin of this PL behavior of the NSs.

Keeping the sub-band-gap energy of light emission, it can be hypothesized that the band-to-band transition is mediated with some localized energy states inside the material band gap. These states are mainly raised from surface and bulk defect states and imperfections such as grain boundaries [23,25,41–46]. To evaluate the stability of the emission under continuous light irradiation, the dispersed solution of VSe_2 NSs has been placed inside a quartz cuvette and exposed to UV irradiation (8 W, UVLMS-38 EL, 302 nm) from a distance of c.a ~1 cm for about 4 h. As it can be clearly seen from Fig. 5(d), the PL intensity of the sample experiences quite a small reduction after this continuous light irradiation that proves its stability under continuous light irradiation. It should be mentioned at the measurements carried out under the atmospheric conditions. Finally, the excitation-intensity-dependent PL spectra of the synthesized VSe_2 NSs are obtained at room temperature as shown in Fig. 5(e). For this aim, the excitation slit width is adopted at four different widths of 2.5, 5, 10, and 20 nm to tune the output laser power. As it can be clearly seen from this panel, the shape of the spectra is almost same for all the cases where the larger light intensity (which corresponds to wider slit width) makes the emission more intense. Therefore, the nature of the PL is similar for different excitation intensities.

To be able to address the transition from 1T to 2H in the prepared samples, we performed Raman spectroscopy to understand the difference between VSe_2 bulk and produced NSs. Figure 6 reveals the spectra for bulk and NS samples. The Raman pattern for the rock material shows a distinct peak at 206 cm^{-1} attributed to the Raman active A_{1g} mode of 1T-VSe_2, which is in perfect agreement with previous findings [47,68]. However, the NS structure shows two peaks that are narrower than that of the bulk one. Previous studies on MoS_2 have revealed that the existence of an E_{2g} resonant mode at the lower energies, which is the characteristic peak of 2H-MoS_2, indicates the conversion from the 1T to 2H phase [74,75]. The same hypothesis can be also applied to our case. Moreover, the existance of an intense peak at 234 cm^{-1} shows the formation of V_xO_y [47,68], which is confirmed by XPS results as well.

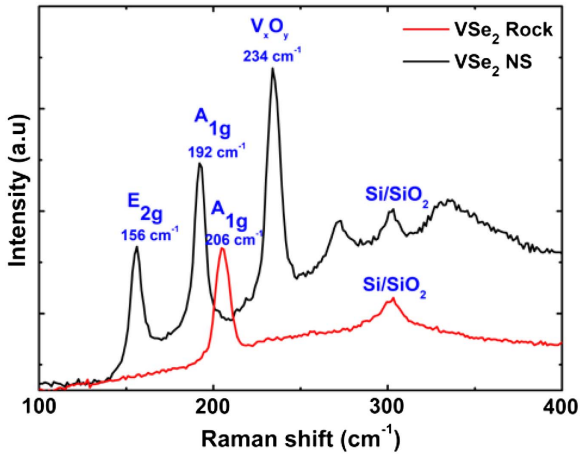

Fig. 6. Raman spectra of the VSe_2 rock and prepared NS samples.

To elaborate the type and density of defect states, XPS measurements are conducted on the rock, NP, and NS samples. For this aim, a couple of drops from the solution are drop-casted onto a copper grid in the both cases and the obtained spectra have been compared with that of VSe_2 rock. Figures 7(a)–7(c) depicts the deconvoluted V 2p and O 1s spectra for all three cases. As Fig. 7(a) implies, the V 2p spectrum of the rock comprises two distinct doublets. The first doublet belongs to $V2p_{3/2} = 513.2$ eV and $V2p_{1/2} = 520.6$ eV orbitals of VSe_2 that is in agreement with the reported values of previous papers [47,68]. The second doublet with binding energies of $V2p_{3/2} = 515.7$ eV and $V2p_{1/2} = 522.5$ eV originates from surface oxides, i.e., V_xO_y (such as V_2O_5), which is due to the surface oxidation of the rock and matches with the energy levels of previous studies [68]. The existence of this oxide has also been confirmed from the O 1s spectrum, which appears as a small weak peak at 531.7 eV. Therefore, these results show dominant peaks related to VSe_2 with a partial surface oxidation. However, the story is very different for the case of NPs and NSs. Although the V 2p spectra of these two samples also comprise two different doublets, the portion of oxide-related peaks is dominant in this case. As Fig. 7(b) represents, the VSe_2 corresponded doublet is located at binding energies of $V2p_{3/2} = 515.8$ eV and $V2p_{1/2} = 523.7$ eV, while the ones belonged to V_xO_y appear at energy values of $V2p_{3/2} = 517.3$ eV and $V2p_{1/2} = 525.2$ eV. When comparing these numbers with those of rock signals, one can clearly see that not only the peaks' dominancy has been exchanged (between VSe_2 and V_xO_y) but also the energetic positions of the orbitals have shifted to larger values. Looking back onto our previous results that propose a phase transformation from 1T- to 2H-VSe_2, this shift can also be assigned to this phenomenon. Previous studies on MoS_2 have proved that the binding energy of the 2H-Mo 3d doublet emerges at larger binding energies compared to that of 1T-Mo 3D ones. Therefore, this is also in line with our previous findings that predict the transformation of 1T-VSe_2 to 2H-VSe_2 upon exposure with a laser IR beam. Looking at the PLA method principles, we can also find that the dominancy of oxide peaks is an expected condition. During the PLA process, intense IR beam impinges on the bulk rock and at the high laser fluence levels, and extreme local heating is created at the surface and its vicinity. This high temperature leads to adiabatic melting/re-solidifying and, consequently, the NP gets oxidized and several imperfections and grain boundaries appear at the surface of VSe_2 NPs. As we continue this ablation process for a relatively large number of cycles, the NPs experience multiple surface reconstructions and, consequently, several surface and bulk defects emerge. Taking the high thermal conductivity of VSe_2, these reconstructions would also occur in its bulk. To be able to distinguish between the formation of oxide

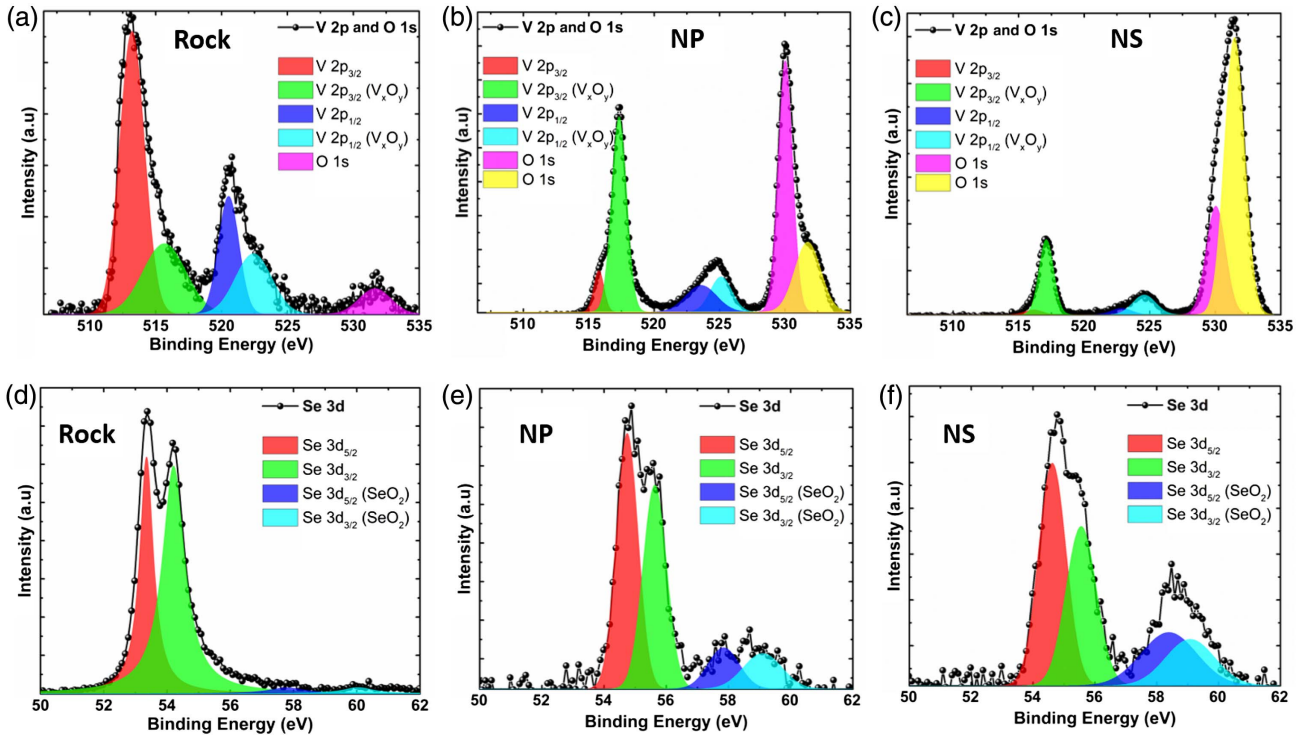

Fig. 7. V 2p-O 1s and Se 3d spectra of the VSe_2 (a),(d) rock, and the prepared (b),(e) NP and (c),(f) NS samples. All spectra have been deconvoluted to multiple peaks.

layer and defect states, we can look at the O 1s spectra of the samples. As it can be explored, the O 1s spectra for both NP and NS solutions are made of two peaks. The first peak that is located at lower energies (530 eV) corresponds to the lattice oxygen of V_2O_5. However, the shoulder positioned at a higher energy of 531.8 eV shows the existence of chemisorbed oxygen species on the sample. This has been proved in several previous studies [76–79]. Based on the calculation of free energy by the classical nucleation theory, most of the water-derived hydroxyl groups, such as OH radicals and H_2O, have a high tendency to be chemisorbed near imperfections, such as defects (like vacancy levels) and grain boundaries. Therefore, it can be speculated that the strength of this peak is a measure of the defect states' density. Based on previous reports, the most common defect states in a TMD structure are chalcogen vacancies that are supposed to be active sites of the materials [25,29,41,42]. Therefore, it can be concluded that during the formation of NP by the PLA method, several Se vacancies will result in the bulk and surface of the nanostructure. As we break these NPs to NS units, the active surface area of the material gets larger, and all the defect states at the bulk of the design become surface defects. Therefore, it is expected that higher levels of defect states will be created in the case of VSe_2 NSs. This can be confirmed by scrutinizing the V 2p and O 1s spectra of the NSs, which are depicted in Fig. 7(c). According to this panel, the V 2p orbitals have the same trend and dominancy as the case NPs. However, the main difference between NPs and NSs raises from their O 1s peaks. Two deconvoluted peaks show that, unlike the NPs' O 1s spectra, the peak related to chemisorbed oxygen radicals is dominant over the lattice oxygen peak for NSs. To have a better qualitative comparision on the density of Se vacancies, the area under the chemisorbed related peak is divided by the sum of areas corresponding to VSe_2 doublets, located at binding energies of 515.8 eV and 523.7 eV. Our calculations reveal that while this ratio is 0.76 for the NP case, it increases to the value of 3.47 for the NS sample. Therefore, comparing all the data, NS structure has the highest level of surface-defect states that are thought to be Se vacancies. This hypothesis is also in agreement with the PL spectra of these two samples. As already explained, the PL signals for both of these cases show the same pattern but with a different strength. Therefore, it was envisioned that similar physics is responsible for emission in both cases. Based on the current results, the surface defects are the active sites for PL in both NPs and NSs, and higher concentration of these defects in the NS sample makes its PL intensity stronger. It should be mentioned that besides the vacancy levels, the active edge sites and chemisorbed groups can also impose a critical role on the PL performance of the NS design. About the chemical groups, as already mentioned in the paper, the defect sites are energetically favorable for molecular adsorption and chemical functionalization. It has been found that these chemisorbed groups can bond to the material's surface and deplete the excess electrons at the vicinity of the surface [46]. Depletion of the electrons can suppress the thermally activated nonradiative recombination, and the excitons at defects sites are dominated by radiative recombination at room temperature, resulting in a high PL quantum efficiency. Moreover, another active site for PL of VSe_2 can be the edge sites. However, as revealed by XPS

measurements, the density of Se vacancy traps is quite large in the case of the NS structure. Considering the relatively large size of NSs and their low density of edges (as shown in the TEM images), it can be speculated that the emission is mainly due to defect states created through the plane of the NSs rather than their edge active sites. Moreover, the Se 3D spectra for all three cases are also shown in Figs. 7(d)–7(f). For all of the cases, there are two doublets: (1) the lower-energy doublet comprising two peaks that are due to the spin orbit splitting of the Se 3D level of VSe_2 [47,68], and (2) the higher-energy doublet that matches Se 3D binding energies of SeO_x [80,81]. According to the obtained results, while there is a negligible trace of SeO_x formation, these peaks are much stronger for NP and NS samples, which are again due to the local heating in the PLA process.

4. CONCLUSIONS

In summary, this study proposes a facial, contaminant-free, and large-scale-compatible approach to synthesize luminescent VSe_2 NSs that has not been reported before. This paper, for the first time, demonstrates the possibility of attaining photoluminescence from VSe_2 NSs. Based on the findings of this paper, the photoluminescence of these NSs originates from the existence of surface-defect states in the materials. These defect states have been produced during the PLA process. Moreover, it was speculated that the use of IR radiation through the PLA method triggers the phase transformation from 1T- to 2H-VSe_2. Our findings prove that VSe_2 has not only superior electrical properties, but it can also be a promising semiconductor for photovoltaics, LED, and other optoelectronic applications.

Funding. Türkiye Bilimsel ve Teknolojik Araştirma Kurumu (TüBITAK) (113E331, 114E374, 115F560).

Acknowledgment. E. Ozbay also acknowledges partial support from the TUBA. Authors also thank Dr. Serkan Kasirga for supplying the material.

REFERENCES

1. A. K. Geim, "Graphene: status and prospects," Science **324**, 1530–1534 (2009).
2. Y. Zhu, S. Murali, W. Cai, X. Li, J. W. Suk, J. R. Potts, and R. S. Ruoff, "Graphene and graphene oxide: synthesis, properties, and applications," Adv. Mater. **22**, 3906–3924 (2010).
3. M. J. Allen, V. C. Tung, and R. B. Kaner, "Honeycomb carbon: a study of graphene," Chem. Rev. **110**, 132–145 (2010).
4. Q. H. Wang, K. Kalantar-Zadeh, A. Kis, J. N. Coleman, and M. S. Strano, "Electronics and optoelectronics of two-dimensional transition metal dichalcogenides," Nat. Nanotechnol. **7**, 699–712 (2012).
5. M. Chhowalla, H. S. Shin, G. Eda, L. J. Li, K. P. Loh, and H. Zhang, "The chemistry of two-dimensional layered transition metal dichalcogenide nanosheets," Nat. Chem. **5**, 263–275 (2013).
6. D. Jariwala, V. K. Sangwan, L. J. Lauhon, T. J. Marks, and M. C. Hersam, "Emerging device applications for semiconducting two-dimensional transition metal dichalcogenides," ACS Nano **8**, 1102–1120 (2014).
7. Y. Liu, N. O. Weiss, X. Duan, H.-C. Cheng, Y. Huang, and X. Duan, "Van der Waals heterostructures and devices," Nat. Rev. Mater. **1**, 16042 (2016).
8. C. Luo, C. Wang, X. Wu, J. Zhang, and J. Chu, "*In situ* transmission electron microscopy characterization and manipulation of two-dimensional layered materials beyond graphene," Small **13**, 1604259 (2017).
9. M. M. Furchi, A. Pospischil, F. Libisch, J. Burgdo, and T. Mueller, "Photovoltaic effect in an electrically tunable van der Waals heterojunction," Nano Lett. **14**, 4785–4791 (2014).
10. M. Bernardi, M. Palummo, C. Grossman, and R. Scienti, "Extraordinary sunlight absorption and one nanometer thick photovoltaics using two-dimensional monolayer materials," Nano Lett. **13**, 3664–3670 (2013).
11. N. Balis, E. Stratakis, and E. Kymakis, "Graphene and transition metal dichalcogenide nanosheets as charge transport layers for solution processed solar cells," Mater. Today **19**, 580–594 (2016).
12. O. Lopez-sanchez, D. Lembke, M. Kayci, A. Radenovic, and A. Kis, "Ultrasensitive photodetectors based on monolayer MoS_2," Nat. Nanotechnol. **8**, 497–501 (2013).
13. D. Kang, M. Kim, J. Shim, J. Jeon, H. Park, W. Jung, H. Yu, C. Pang, S. Lee, and J. Park, "High-performance transition metal dichalcogenide photodetectors enhanced by self-assembled monolayer doping," Adv. Funct. Mater. **25**, 4219–4227 (2015).
14. D. B. Velusamy, R. H. Kim, S. Cha, J. Huh, R. Khazaeinezhad, S. H. Kassani, G. Song, S. M. Cho, S. H. Cho, I. Hwang, J. Lee, K. Oh, H. Choi, and C. Park, "Flexible transition metal dichalcogenide nanosheets for band-selective photodetection," Nat. Commun. **6**, 8063 (2015).
15. F. Withers, O. Del Pozo-Zamudio, A. Mishchenko, A. P. Rooney, A. Gholinia, K. Watanabe, T. Taniguchi, S. J. Haigh, A. K. Geim, A. I. Tartakovskii, and K. S. Novoselov, "Light-emitting diodes by band-structure engineering in van der Waals heterostructures," Nat. Mater. **14**, 301–306 (2015).
16. O. Lopez-Sanchez, E. Alarcon Llado, V. Koman, A. Fontcuberta, I. Morral, A. Radenovic, and A. Kis, "Light generation and harvesting in a van der Waals heterostructure," ACS Nano **8**, 3042–3048 (2014).
17. D. M. Andoshe, J. M. Jeon, S. Y. Kim, and H. W. Jang, "Two-dimensional transition metal dichalcogenide nanomaterials for solar water splitting," Electron. Mater. Lett. **11**, 323–335 (2015).
18. M. Pumera, Z. Sofer, and A. Ambrosi, "Layered transition metal dichalcogenides for electrochemical energy generation and storage," J. Mater. Chem. A **2**, 8981–8987 (2014).
19. Y. Hou, X. Zhuang, and X. Feng, "Recent advances in earth-abundant heterogeneous electrocatalysts for photoelectrochemical water splitting," Small Methods **1**, 1700090 (2017).
20. W. Peng, Y. Li, F. Zhang, G. Zhang, and X. Fan, "Roles of two-dimensional transition metal dichalcogenides as cocatalysts in photocatalytic hydrogen evolution and environmental remediation," Ind. Eng. Chem. Res. **56**, 4611–4626 (2017).
21. Y. Wan, H. Zhang, K. Zhang, Y. Wang, B. Sheng, X. Wang, and L. Dai, "Large-scale synthesis and systematic photoluminescence properties of monolayer MoS_2 on fused silica," ACS Appl. Mater. Interfaces **8**, 18570–18576 (2016).
22. K. Mak, C. Lee, J. Hone, J. Shan, and T. Heinz, "Atomically thin MoS_2: a new direct-gap semiconductor," Phys. Rev. Lett. **105**, 136805 (2010).
23. Z. He, X. Wang, W. Xu, Y. Zhou, Y. Sheng, Y. Rong, J. M. Smith, and J. H. Warner, "Revealing defect-state photoluminescence in monolayer WS_2 by cryogenic laser processing," ACS Nano **10**, 5847–5855 (2016).
24. H. R. Gutierrez, N. Perea-Lopez, A. L. Elias, A. Berkdemir, B. Wang, R. Lv, F. Lopez-Urias, V. H. Crespi, H. Terrones, and M. Terrones, "Extraordinary room-temperature photoluminescence in WS_2 triangular monolayers," Nano Lett. **13**, 3447–3454 (2013).
25. Z. Wu, W. Zhao, J. Jiang, T. Zheng, Y. You, J. Lu, and Z. Ni, "Defect activated photoluminescence in WSe_2 monolayer," J. Phys. Chem. C **121**, 12294–12299 (2017).
26. C. Ruppert, O. B. Aslan, and T. F. Heinz, "Optical properties and band gap of single- and few-layer $MoTe_2$ crystals," Nano Lett. **14**, 6231–6236 (2014).
27. I. G. Lezama, A. Arora, A. Ubaldini, C. Barreteau, E. Giannini, M. Potemski, and A. F. Morpurgo, "Indirect-to-direct band-gap crossover in few-layer $MoTe_2$," Nano Lett. **15**, 2336–2342 (2015).

28. G. Froehlicher, E. Lorchat, and S. Berciaud, "Direct versus indirect band gap emission and exciton-exciton annihilation in atomically thin molybdenum ditelluride ($MoTe_2$)," Phys. Rev. B **94**, 085429 (2016).
29. H. V. Han, A. Y. Lu, L. S. Lu, J. K. Huang, H. Li, C. L. Hsu, Y. C. Lin, M. H. Chiu, K. Suenaga, C. W. Chu, H. C. Kuo, W. H. Chang, L. J. Li, and Y. Shi, "Photoluminescence enhancement and structure repairing of monolayer $MoSe_2$ by hydrohalic acid treatment," ACS Nano **10**, 1454–1461 (2016).
30. N. Peimyoo, W. Yang, J. Shang, X. Shen, Y. Wang, and T. Yu, "Chemically driven tunable light emission of charged and neutral excitons in monolayer WS_2," ACS Nano **8**, 11320–11329 (2014).
31. S. Mouri, Y. Miyauchi, and K. Matsuda, "Tunable photoluminescence of monolayer MoS_2 via chemical doping," Nano Lett. **13**, 5944–5948 (2013).
32. B. Mukherjee, N. Kaushik, R. P. N. Tripathi, A. M. Joseph, P. K. Mohapatra, S. Dhar, B. P. Singh, G. V. P. Kumar, E. Simsek, and S. Lodha, "Exciton emission intensity modulation of monolayer MoS_2 via Au plasmon coupling," Sci. Rep. **7**, 41175 (2017).
33. H. Li, X. Duan, X. Wu, X. Zhuang, H. Zhou, Q. Zhang, X. Zhu, W. Hu, P. Ren, P. Guo, L. Ma, X. Fan, X. Wang, J. Xu, A. Pan, and X. Duan, "Growth of alloy $MoS_{2x}Se_{2(1-x)}$nanosheets with fully tunable chemical compositions and optical properties," J. Am. Chem. Soc. **136**, 3756–3759 (2014).
34. M. D. Tran, J. H. Kim, and Y. H. Lee, "Tailoring photoluminescence of monolayer transition metal dichalcogenides," Curr. Appl. Phys. **16**, 1159–1174 (2016).
35. S. Susarla, A. Kutana, J. A. Hachtel, V. Kochat, A. Apte, R. Vajtai, J. C. Idrobo, B. I. Yakobson, C. S. Tiwary, and P. M. Ajayan, "Quaternary 2D transition metal dichalcogenides (TMDs) with tunable bandgap," Adv. Mater. **29**, 1702457 (2017).
36. Z. Wang, Z. Dong, Y. Gu, Y. H. Chang, L. Zhang, L. J. Li, W. Zhao, G. Eda, W. Zhang, G. Grinblat, S. A. Maier, J. K. W. Yang, C. W. Qiu, and A. T. S. Wee, "Giant photoluminescence enhancement in tungsten-diselenide-gold plasmonic hybrid structures," Nat. Commun. **7**, 11283 (2016).
37. E. Palacios, S. Park, S. Butun, L. Lauhon, and K. Aydin, "Enhanced radiative emission from monolayer MoS_2 films using a single plasmonic dimer nanoantenna," Appl. Phys. Lett. **111**, 031101 (2017).
38. S. Wu, S. Buckley, A. M. Jones, J. S. Ross, N. J. Ghimire, J. Yan, D. G. Mandrus, W. Yao, F. Hatami, J. Vučković, A. Majumdar, and X. Xu, "Control of two-dimensional excitonic light emission via photonic crystal," 2D Mater. **1**, 011001 (2014).
39. X. Gan, Y. Gao, K. F. Mak, X. Yao, R.-J. Shiue, A. van der Zande, M. Trusheim, F. Hatami, T. F. Heinz, J. Hone, and D. Englund, "Controlling the spontaneous emission rate of monolayer MoS_2 in a photonic crystal nanocavity," Appl. Phys. Lett. **103**, 181119 (2013).
40. J. Lee, J. Huang, B. G. Sumpter, and M. Yoon, "Strain-engineered optoelectronic properties of 2D transition metal dichalcogenide lateral heterostructures," 2D Mater. **4**, 021016 (2017).
41. Z. Lin, A. Mccreary, U. Wurstbauer, B. Miller, J. S. Ponraj, Z. Xu, Z. Lin, B. R. Carvalho, E. Kahn, R. Lv, R. Rao, and H. Terrones, "Defect engineering of two-dimensional transition metal dichalcogenides," 2D Mater. **3**, 022002 (2016).
42. P. K. Chow, R. B. Jacobs-Gedrim, J. Gao, T. Lu, B. Yu, and H. Terrones, "Defect-induced photoluminescence in monolayer semiconducting transition metal dichalcogenides," ACS Nano **9**, 1520–1527 (2015).
43. V. Carozo, Y. Wang, K. Fujisawa, B. R. Carvalho, A. Mccreary, S. Feng, Z. Lin, C. Zhou, N. Perea-López, A. L. Elías, B. Kabius, V. H. Crespi, and M. Terrones, "Optical identification of sulfur vacancies: bound excitons at the edges of monolayer tungsten disulfide," Sci. Adv. **3**, e1602813 (2017).
44. A. Veamatahau, B. Jiang, T. Seifert, S. Makuta, K. Latham, M. Kanehara, T. Teranishi, and Y. Tachibana, "Origin of surface trap states in CdS quantum dots: relationship between size dependent photoluminescence and sulfur vacancy trap states," Phys. Chem. Chem. Phys. **17**, 2850–2858 (2015).
45. H. Y. Jeong, S. Y. Lee, T. H. Ly, G. H. Han, H. Kim, H. Nam, Z. Jiong, B. G. Shin, S. J. Yun, J. Kim, U. J. Kim, S. Hwang, and Y. H. Lee, "Visualizing point defects in transition-metal dichalcogenides using optical microscopy," ACS Nano **10**, 770–777 (2016).
46. H. Nan, Z. Wang, W. Wang, Z. Liang, Y. Lu, Q. Chen, D. He, P. Tan, F. Miao, X. Wang, J. Wang, and Z. Ni, "Strong photoluminescence enhancement of MoS_2 through defect engineering and oxygen bonding," ACS Nano **8**, 5738–5745 (2014).
47. Z. Zhang, J. Niu, P. Yang, Y. Gong, Q. Ji, J. Shi, Q. Fang, S. Jiang, H. Li, X. Zhou, L. Gu, X. Wu, and Y. Zhang, "Van der Waals epitaxial growth of 2D metallic vanadium diselenide single crystals and their extra-high electrical conductivity," Adv. Mater. **29**, 1702359 (2017).
48. H. Zhang, L. Sun, Y. Dai, C. Tong, and X. Han, "Tunable electronic and magnetic properties from structure phase transition of layered vanadium diselenide," J. Wuhan Univ. Technol. Mater. Sci. Ed. **32**, 574–578 (2017).
49. Z. I. Popov, N. S. Mikhaleva, M. A. Visotin, A. A. Kuzubov, S. Entani, H. Naramoto, S. Sakai, P. B. Sorokin, and P. V. Avramov, "The electronic structure and spin states of 2D graphene/VX_2 (X = S, Se) heterostructures," Phys. Chem. Chem. Phys. **18**, 33047–33052 (2016).
50. Á. Pásztor, A. Scarfato, C. Barreteau, E. Giannini, and C. Renner, "Dimensional crossover of the charge density wave transition in thin exfoliated VSe_2," 2D Mater. **4**, 041005 (2017).
51. W. Tong, S. Gong, X. Wan, and C. Duan, "Concepts of ferrovalley material and anomalous valley Hall effect," Nat. Commun. **7**, 13612 (2016).
52. H.-R. Fuh, B. Yan, S.-C. Wu, C. Felser, and C.-R. Chang, "Metal-insulator transition and the anomalous Hall effect in the layered magnetic materials VS_2 and VSe_2," New J. Phys. **18**, 113038 (2016).
53. K. Xu, P. Chen, X. Li, C. Wu, Y. Guo, J. Zhao, and X. Wu, "Ultrathin nanosheets of vanadium diselenide: a metallic two-dimensional material with ferromagnetic charge-density-wave behavior," Angew. Chem. **52**, 10477–10481 (2013).
54. M. Yan, X. Pan, P. Wang, F. Chen, L. He, G. Jiang, J. Wang, J. Z. Liu, X. Xu, X. Liao, J. Yang, and L. Mai, "Field-effect tuned adsorption dynamics of VSe_2 nanosheets for enhanced hydrogen evolution reaction," Nano Lett. **17**, 4109–4115 (2017).
55. W. Zhao, B. Dong, Z. Guo, G. Su, R. Gao, W. Wang, and L. Cao, "Colloidal synthesis of VSe_2 single-layer nanosheets as novel electrocatalysts for the hydrogen evolution reaction," Chem. Commun. **52**, 9228–9231 (2016).
56. X. Chia, A. Ambrosi, P. Lazar, Z. Sofer, and M. Pumera, "Electrocatalysis of layered Group 5 metallic transition metal dichalcogenides (MX_2, M = V, Nb, and Ta; X = S, Se, and Te)," J. Mater. Chem. A **4**, 14241–14253 (2016).
57. Y. Wang, Z. Sofer, J. Luxa, and M. Pumera, "Lithium exfoliated vanadium dichalcogenides (VS_2, VSe_2, VTe_2) exhibit dramatically different properties from their bulk counterparts," Adv. Mater. Interfaces **3**, 1600433 (2016).
58. T. G. Ulusoy Ghobadi, B. Patil, F. Karadas, A. K. Okyay, and E. Yilmaz, "Catalytic properties of vanadium diselenide: a comprehensive study on its electrocatalytic performance in alkaline, neutral, and acidic media," ACS Omega **2**, 8319–8329 (2017).
59. S. He, H. Lin, L. Qin, Z. Mao, H. He, Y. Li, and Q. Li, "Synthesis, stability, and intrinsic photocatalytic properties of vanadium diselenide," J. Mater. Chem. A **5**, 2163–2171 (2017).
60. X. Fan, P. Xu, D. Zhou, Y. Sun, Y. C. Li, M. A. T. Nguyen, M. Terrones, and T. E. Mallouk, "Fast and efficient preparation of exfoliated 2H MoS_2 nanosheets by sonication-assisted lithium intercalation and infrared laser-induced 1T to 2H phase reversion," Nano Lett. **15**, 5956–5960 (2015).
61. T. P. Nguyen, W. Sohn, J. H. Oh, H. W. Jang, and S. Y. Kim, "Size-dependent properties of two-dimensional MoS_2 and WS_2," J. Phys. Chem. C **120**, 10078–10085 (2016).
62. V. Štengl and J. Henych, "Strongly luminescent monolayered MoS_2 prepared by effective ultrasound exfoliation," Nanoscale **5**, 3387–3394 (2013).
63. M. M. Bernal, L. Álvarez, E. Giovanelli, A. Arnáiz, L. Ruiz-González, S. Casado, D. Granados, A. M. Pizarro, A. Castellanos-Gomez, and E. M. Pérez, "Luminescent transition metal dichalcogenide nanosheets through one-step liquid phase exfoliation," 2D Mater. **3**, 035014 (2016).
64. C. Y. Luan, S. Xie, C. Ma, S. Wang, Y. Kong, and M. Xu, "Elucidation of luminescent mechanisms of size-controllable $MoSe_2$ quantum dots," Appl. Phys. Lett. **111**, 073105 (2017).

65. K. S. Nikonov, M. N. Brekhovskikh, A. V. Egorysheva, T. K. Menshchikova, and V. A. Fedorov, "Chemical vapor transport growth of vanadium (IV) selenide and vanadium (IV) telluride single crystals," Inorg. Mater. **53**, 1126–1130 (2017).
66. A. Gustinetti, G. Campagnoli, H. Mutka, P. Molinie, R. H. Friend, D. Jerome, A. Nader, and A. Leblanc, "The characterisation of VSe_2: a study of the thermal expansion," J. Phys. C **14**, L609–L615 (1981).
67. E. Spiecker, A. K. Schmid, A. M. Minor, U. Dahmen, S. Hollensteiner, and W. Ja, "Self-assembled nanofold network formation on layered crystal surfaces during metal intercalation," Phys. Rev. Lett. **96**, 086401 (2006).
68. N. D. Boscher, C. S. Blackman, C. J. Carmalt, I. P. Parkin, and A. G. Prieto, "Atmospheric pressure chemical vapour deposition of vanadium diselenide thin films," Appl. Surf. Sci. **253**, 6041–6046 (2007).
69. T. Oztas, H. S. Sen, E. Durgun, and B. Ortaç, "Synthesis of colloidal 2D/3D MoS_2 nanostructures by pulsed laser ablation in an organic liquid environment," J. Phys. Chem. C **118**, 30120–30126 (2014).
70. H. G. Baldoví, M. Latorre-Sánchez, I. Esteve-Adell, A. Khan, A. M. Asiri, S. A. Kosa, and H. Garcia, "Generation of MoS_2 quantum dots by laser ablation of MoS_2 particles in suspension and their photocatalytic activity for H_2 generation," J. Nanopart. Res. **18**, 240 (2016).
71. L. Zhou, H. Zhang, H. Bao, G. Liu, Y. Li, and W. Cai, "Onion-structured spherical MoS_2 nanoparticles induced by laser ablation in water and liquid droplets' radial solidification/oriented growth mechanism," J. Phys. Chem. C **121**, 23233–23239 (2017).
72. S. R. M. Santiago, T. N. Lin, C. T. Yuan, J. L. Shen, H. Y. Huang, and C. A. J. Lin, "Origin of tunable photoluminescence from graphene quantum dots synthesized via pulsed laser ablation," Phys. Chem. Chem. Phys. **18**, 22599–22605 (2016).
73. T. G. Ulusoy Ghobadi, A. Ghobadi, T. Okyay, K. Topalli, and A. K. Okyay, "Controlling luminescent silicon nanoparticle emission produced by nanosecond pulsed laser ablation: role of interface defect states and crystallinity phase," RSC Adv. **6**, 112520 (2016).
74. C. Guo, J. Pan, H. Li, T. Lin, P. Liu, C. Song, D. Wang, G. Mu, X. Lai, H. Zhang, W. Zhou, M. Chen, and F. Huang, "Observation of superconductivity in 1T′-MoS_2 nanosheets," J. Mater. Chem. C **5**, 10855–10860 (2017).
75. S. Jiménez Sandoval, D. Yang, R. Frindt, and J. Irwin, "Raman study and lattice dynamics of single molecular layers of MoS_2," Phys. Rev. B **44**, 3955–3962 (1991).
76. C. Lin, A. Posadas, T. Hadamek, and A. A. Demkov, "Final-state effect on X-ray photoelectron spectrum of nominally d^1 and n-doped d^0 transition-metal oxides," Phys. Rev. B **92**, 035110 (2015).
77. D. Sethi, N. Jada, A. Tiwari, S. Ramasamy, T. Dash, and S. Pandey, "Photocatalytic destruction of *Escherichia coli* in water by V_2O_5/TiO_2," J. Photochem. Photobiol. B **144**, 68–74 (2015).
78. A. Ghobadi, H. I. Yavuz, T. G. Ulusoy, K. C. Icli, M. Ozenbas, and A. K. Okyay, "Enhanced performance of nanowire-based all-TiO_2 solar cells using subnanometer-thick atomic layer deposited ZnO embedded layer," Electrochim. Acta **157**, 23–30 (2015).
79. T. G. Ulusoy, A. Ghobadi, and A. K. Okyay, "Surface engineered angstrom thick ZnO-sheathed TiO_2 nanowires as photoanodes for performance enhanced dye-sensitized solar cells," J. Mater. Chem. A **2**, 16867–16876 (2014).
80. E. New, I. Hancox, L. A. Rochford, M. Walker, A. Dearden, C. F. Mcconville, and T. S. Jones, "Organic photovoltaic cells utilising ZnO electron extraction layers produced through thermal conversion of ZnSe," J. Mater. Chem. A **2**, 19201–19207 (2014).
81. M. A. Morris, M. A. Morris, N. Petkov, and J. D. Holmes, "Resist-substrate interface tailoring for generating high-density arrays of Ge and Bi_2Se_3 nanowires by electron beam lithography," J. Vac. Sci. Technol. B **30**, 041602 (2012).